A coarse-graining approach for dilepton production at SPS energies

Stephan Endres,* Hendrik van Hees, Janus Weil, and Marcus Bleicher
Frankfurt Institute for Advanced Studies, Ruth-Moufang-Strasse 1, D-60438 Frankfurt, Germany and
Institut für Theoretische Physik, Universität Frankfurt,
Max-von-Laue-Strasse 1, D-60438 Frankfurt, Germany
(Dated: April 24, 2015)

Coarse-grained output from transport calculations is used to determine thermal dilepton emission rates by applying medium-modified spectral functions from thermal quantum field theoretical models. By averaging over an ensemble of events generated with the UrQMD transport model, we extract the local thermodynamic properties at each time step of the calculation. With an equation of state the temperature T and chemical potential μ_B can be determined. The approach goes beyond simplified fireball models of the bulk-medium evolution by treating the full (3+1)-dimensional expansion of the system with realistic time and density profiles. For the calculation of thermal dilepton rates we use the in-medium spectral function of the ρ meson developed by Rapp and Wambach and consider thermal QGP and multi-pion contributions as well. The approach is applied to the evaluation of dimuon production in In+In collisions at top SPS energy. Comparison to the experimental results of the NA60 experiment shows good agreement of this ansatz. We find that the experimentally observed low-mass dilepton excess in the mass region from 0.2 to 0.6 GeV can be explained by a broadening of the ρ spectral function with a small mass shift. In contrast, the intermediate mass region ($M > 1.5$ GeV) is dominated by a contribution from the quark-gluon plasma. These findings agree with previous calculations with fireball parametrizations. This agreement in spite of differences in the reaction dynamics between both approaches indicates that the time-integrated dilepton spectra are not very sensitive to details of the space-time evolution of the collision.

PACS numbers: 24.10.Lx, 25.75.-q, 25.75.Dw, 25.75.Cj
Keywords: Monte Carlo simulations, Relativistic heavy-ion collisions, Particle and resonance production, Dilepton production

arXiv:1412.1965v3 [nucl-th] 23 Apr 2015

I. INTRODUCTION

The in-medium properties of hadrons have been a field of intense studies in theory and experiment over the last years [1–6]. One aims to learn more about the phase diagram of QCD and especially to find hints for a possible restoration of chiral symmetry. For such studies of hot and dense nuclear matter, dileptons are a unique tool. As they do not interact strongly, they suffer only negligible final-state interactions with the medium and thus provide insight into the spectral properties of their source, i.e., dileptons provide a direct view on the in-medium electromagnetic current-current correlation function of QCD matter during the entire history of the collision, from first nucleon-nucleon reactions to final freeze-out [2, 7, 8]. However, this advantage also comes with a drawback. As we only get time-integrated spectra over the whole space-time evolution of a nuclear reaction, it is difficult to disentangle the various contributing processes which requires a realistic description of all collision stages.

Considering the different experimental efforts to investigate dilepton production in heavy-ion collisions, the NA60 experiment plays a prominent role. It measured dimuons in heavy-ion collisions at top SPS energies with an unprecedented precision. The high accuracy of the measurement enabled the subtraction of the background contributions (long-lived mesons as η, η', ω, ϕ) from the dilepton spectra. Consequently, the NA60 results deliver direct insight into the in-medium effects on the ρ spectral function in the low-mass region up to 1 GeV [9–11] and the thermal dimuon emission in the intermediate mass region [12]. A main finding was a large excess of lepton pairs in the mass region 0.2-0.4 GeV, which confirmed the previous results by CERES [13]. Theoretical studies showed that this excess can be explained by a strong broadening of the ρ spectral function with small mass shifts [14–17].

In general there exist two different types of approaches to describe heavy-ion collisions, microscopic and macroscopic ones. The microscopic models, e.g., transport models as UrQMD [18, 19], HSD [20] or GiBUU [21], focus on the description of all the subsequent hadron-hadron collisions (respectively interactions of partons), according to the Boltzmann equation. The difficulty here is to implement in-medium effects in such a microscopic non-equilibrium approach which is highly non-trivial, but nevertheless some investigations on that issue have been conducted successfully [22–31]. On the other hand, in macroscopic models such as thermal fireball models [32] or hydrodynamics [16, 33–37], the application of in-medium hadronic spectral functions from thermal quantum-field theory is straightforward. However, due to their plainness the fireball parametrizations might oversimplify the real dynamics of a nuclear reaction, and hydrodynamical simulations may not be applicable to the less hot and dense medium created at lower collision energies. Furthermore, the creation of

* endres@th.physik.uni-frankfurt.de

an equilibrium state of hot and dense matter after quite short formation times is usually assumed in these models whereas the results from microscopic investigations indicate the importance of non-equilibrium effects during the evolution of a heavy-ion collision [38].

Combining a realistic (3+1)-dimensional expansion of the system with full in-medium spectral functions for the thermal emission of dileptons is yet an important challenge for theory. One approach that has proven successful in explaining the NA60 results is the investigation of dilepton production with a hybrid model [39]. It combines a cascade calculation of the reaction dynamics with thermal emission from an intermediate hydrodynamic stage. However, as all hydro-approaches it is only working properly for sufficiently large collision energies. Furthermore, the hybrid-approach falls into three different stages, a pre-hydro phase, the hydrodynamic stage and the transport phase after particlization. An application of in-medium spectral functions hereby only applies for the rather short hydro stage.

For the study presented in this paper we follow an approach which uses a microscopic description for the whole evolution of the collision and enables the use of in-medium spectral functions from thermal quantum-field theoretical models at all stages. Taking a large number of events generated with the Ultra-relativistic Quantum Molecular Dynamics (UrQMD) model, we place the output on a space-time grid and extract the local temperature and baryon chemical potential by averaging energy and baryon density over the events (i.e., we "coarse-grain" the microscopic results) which allows for the calculation of local thermal dilepton emission. This ansatz was previously proposed and used to calculate hadron, dilepton and photon spectra [40]. For the present work we modify the approach to include also the very initial stage of the reaction (which was separately treated in the cited work) and account for non-equilibrium effects with respect to the pion dynamics. Additionally we include non-thermal contributions to really cover the whole evolution of the nucleus-nucleus reaction.

This paper is structured as follows. In Section II the coarse-graining approach is described in detail and the different contributions to the dilepton emission included in the model are introduced. Subsequently we present the results for the space-time evolution of the nuclear reaction in Section III A followed by the dilepton invariant-mass and transverse-momentum spectra, which we compare to the experimental results in III B. Finally, in Section IV a summary and an outlook on further studies is given.

II. THE MODEL

A. The coarse-graining approach

The underlying input for our calculations stems from the Ultra-relativistic Quantum Molecular Dynamics Approach (UrQMD) [18, 19, 41, 42]. It is a non-equilibrium transport approach that includes all hadronic resonance states up to a mass of 2.2 GeV and constitutes an effective solution of the relativistic Boltzmann equation. A heavy-ion collision is simulated such that all hadrons are propagated on classical trajectories in combination with elastic and inelastic binary scatterings and resonance decays. At higher energies, string excitation is possible as well. The model has been checked to describe hadronic observables up to RHIC energies with good accuracy [41]. For the further investigations we use the UrQMD output in time steps. This provides positions, momenta, and energies of all particles and resonances at that specific moment in time. The size of each time step for the present calculations is chosen as $\Delta t = 0.2\,\mathrm{fm}/c$.

In the UrQMD model, the particle distribution function of all hadrons is given by an ensemble of point particles, which at time t are defined by their positions $\vec{x}_h$ and momenta $\vec{p}_h$. Each particle's contribution to the phase-space density is then defined as

$$\delta^{(3)}(\vec{x} - \vec{x}_h(t))\delta^{(3)}(\vec{p} - \vec{p}_h(t)). \tag{1}$$

With a sufficiently large number of events the distribution function $f(\vec{x}, \vec{p}, t)$ takes a smooth form

$$f(\vec{x}, \vec{p}, t) = \left\langle \sum_h \delta^{(3)}(\vec{x} - \vec{x}_h(t))\delta^{(3)}(\vec{p} - \vec{p}_h(t)) \right\rangle. \tag{2}$$

Hereby, the ensemble average $\langle\cdot\rangle$ is taken over simulated events. As the UrQMD model constitutes a non-equilibrium approach, the equilibrium quantities have to be extracted locally at each space-time point. In consequence we set up a grid of small space-time cells with a spatial extension Δx of 0.8 fm and average the UrQMD output for each cell on that grid. One can then determine the energy-momentum tensor $T^{\mu\nu}$ and the baryon four-flow according to the following expressions:

$$\begin{aligned} T^{\mu\nu} &= \int \mathrm{d}^3p \frac{p_\mu p_\nu}{p_0} f(\vec{x}, \vec{p}, t) \\ &= \frac{1}{\Delta V} \left\langle \sum_{i=1}^{N_h \in \Delta V} \frac{p^i_\mu \cdot p^i_\nu}{p^i_0} \right\rangle, \end{aligned} \tag{3}$$

$$\begin{aligned} j^{\mathrm{B}}_\mu &= \int \mathrm{d}^3p \frac{p_\mu}{p_0} f^{\mathrm{B}}(\vec{x}, \vec{p}, t) \\ &= \frac{1}{\Delta V} \left\langle \sum_{i=1}^{N_{\mathrm{B}/\bar{\mathrm{B}}} \in \Delta V} \pm \frac{p^i_\mu}{p^i_0} \right\rangle. \end{aligned} \tag{4}$$

For the net-baryon flow in (4) only the distribution function of baryons and anti-baryons $f^{\mathrm{B}}(\vec{x}, \vec{p}, t)$ is considered, excluding all mesons. Each anti-baryon hereby gives a negative contribution to j^{B}_μ. On the contrary, the distribution function for all hadrons in the cell enters in $T^{\mu\nu}$.

According to Eckart's definition [43] the local rest-frame (LRF) is tied to conserved charges, in our case the net-baryon number. Consequently one has to perform a

Lorentz transformation into the frame, where $\vec{j}^{\rm B} = 0$. The unit vector in direction of the baryon flow takes the form

$$u^\mu = \frac{j^\mu}{(j^\nu j_\nu)^{1/2}} = (\gamma, \gamma\vec{v}), \tag{5}$$

where $u_\mu u^\mu = 1$. With this, the rest-frame values for the baryon and energy density are obtained by

$$\rho_B = j_\mu u^\mu = j^0_{\rm LRF}, \tag{6}$$

$$\varepsilon = u_\mu T^{\mu\nu} u_\nu = T^{00}_{\rm LRF}. \tag{7}$$

B. Equilibration and thermal properties of the cells

For the case of a fully equilibrated ideal fluid the energy-momentum tensor would be completely diagonal in the local rest-frame. An important question is to which extent equilibrium is obtained in the present approach and how one can deal with deviations from it.

In macroscopic descriptions of nuclear reaction dynamics local equilibrium is usually introduced as an ad-hoc assumption. (In fireball models, one even assumes a globally equilibrated system). The equilibration of the system is generally assumed to be very fast (on the scale of 1-2 fm/c), after an initial phase. In contrast, no such hypothesis is made within transport approaches, where only the microscopic interactions between the constituent particles of the medium are described. Furthermore, these approaches implicitly include effects as e.g. viscosities or heat conduction and do not fully account for detailed balance. Consequently, non-equilibrium is the normal case at any stage of the collision. On the other hand, to calculate thermal emission rates for dileptons from many-body quantum-field theoretical models, it is necessary know the temperature and baryochemical potential which are by definition equilibrium properties. But when extracting thermodynamic properties from a transport model one has to deal with the problem that many cells are not found in equilibrium. As the coarse-graining approach aims to treat the entire space-time evolution of the collision, this case has to be handled with special care.

Ideally, if complete local equilibrium is achieved, then in each cell the momentum spectrum and the particle abundances should follow a Maxwell-Jüttner-distribution

$$f_{\rm eq}(p, m_i) = \exp\left(-\frac{\sqrt{p^2 + m_i^2} - \mu}{T}\right), \tag{8}$$

with μ being the chemical potentials for the conserved quantities and T being the temperature. Unfortunately, most of the time this ideal case is not realized during the evolution in the present classical transport simulation. For the present investigation however, the following criteria are more relevant, because they allow to include the deviations from equilibrium.

Using the momentum-space anisotropy to characterize the local kinetic equilibrium, one observes from Fig. 2 that kinetic equilibrium may only be reached after 10 fm/c (see also section III A). The question arises, whether the larger anisotropies of the momentum distribution before 10 fm/c affect the extracted energy densities that are of relevance for our studies. We overcome this problem by employing an anisotropic energy-momentum tensor for the extraction of the energy density, as detailed below. The approach to local chemical equilibrium is more difficult to quantify. Approximate chemical equilibrium may also only be reached towards the end of the reaction. Here we take the chemical off-equilibrium situation into account by extracting a pion chemical potential and employing corresponding fugacity factors.

The findings of the present work are in line with previous detailed studies comparing the particle yields and spectra of the UrQMD transport approach at different times with those of the statistical model [44–46] which showed that it takes roughly 10 fm/c until local kinetic and chemical equilibrium is approximately reached for nucleus-nucleus collisions at SPS energies [38, 47, 48].

In summary, to account for the non-equilibrium effects in the present study, which obviously dominate large parts of the evolution, we will use the following scheme: One (i) considers the pressure (respectively momentum) anisotropies in each cell and applies an approach developed for anisotropic hydrodynamics to extract the effective energy density which is used for all further considerations, (ii) introduces an EoS assuming thermal and chemical equilibrium and (iii) finally extracts a pion chemical potential μ_π which is the non-equilibrium effect with the largest impact on the thermal dilepton rates. These aspects will be considered in detail in the following. However, note that step (i) only accounts for deviations from the purely kinetic condition of isotropic momentum distributions and (iii) accounts for the chemical off-equilibrium of the pions only. Besides, when applying the EoS, kinetic and chemical equilibrium in the end remain an assumption here as in any macroscopic approach.

1. *Kinetic anisotropies*

When considering the kinetic properties of the system, one finds that the underlying transport approach in parts depicts large deviations from pressure isotropy. This is especially important for the early stages of the reaction due to the large initial longitudinal momenta carried by the nucleons of the two nuclei traversing each other. In consequence, the longitudinal pressure is much higher than the transverse pressure. To handle this kinetic off-equilibrium situation, a description developed for anisotropic hydrodynamics is employed [49] which allows for differing longitudinal and transverse pressures. In this case the energy-momentum tensor takes the form

$$T^{\mu\nu} = (\varepsilon + P_\perp)\, u^\mu u^\nu - P_\perp\, g^{\mu\nu} - (P_\perp - P_\parallel) v^\mu v^\nu. \tag{9}$$

Here ε is the energy density, $P_\perp$ and $P_\parallel$ are the pressures perpendicular and in direction of the beam, respectively; u^μ is the fluid four-velocity and v^μ the four-vector of the beam direction. To define realistic values for energy density ε and pressure P in the energy-momentum tensor we introduce an anisotropy parameter

$$x = (P_\parallel / P_\perp)^{3/4} \tag{10}$$

and apply a generalized equation of state [50] according to the following relations

$$\varepsilon_{\rm real} = \varepsilon / r(x), \tag{11}$$
$$P_{\rm real} = P_\perp / [r(x) + 3xr'(x)], \tag{12}$$
$$P_{\rm real} = P_\parallel / [r(x) - 6xr'(x)]. \tag{13}$$

The relaxation function $r(x)$, with its derivative $r'(x)$, characterizes the properties of a system which exhibits a Boltzmann-like pressure anisotropy. It is given by

$$r(x) = \begin{cases} \frac{x^{-1/3}}{2}\left(1 + \frac{x\,\mathrm{artanh}\sqrt{1-x}}{\sqrt{1-x}}\right) \text{ for } x \le 1 \\ \frac{x^{-1/3}}{2}\left(1 + \frac{x\arctan\sqrt{x-1}}{\sqrt{x-1}}\right) \text{ for } x \ge 1 \end{cases} . \tag{14}$$

With this procedure one can translate the anisotropic momentum distribution into a local-equilibrium description that gives a realistic value of ε for our further calculations. This effective model to account for the anisotropic pressure of the cell properties allows to treat the early stage of the reaction in the same way as at later times, when a local kinetic equilibration of the system has set in. However, large differences between the "regular" energy density $\varepsilon = T^{00}$ and the effective density $\varepsilon_{\rm real}$ only show up for the first few fm/c of the evolution of the nuclear reaction. After that time we find the longitudinal and perpendicular pressures being of at least the same order of magnitude and $\varepsilon_{\rm real} \approx \varepsilon$, i.e., no significant deviations from the assumption of isotropic momentum distributions (for details see Section III A and [38]). For all further studies we assume that $\varepsilon_{\rm real}$ represents the energy density of the cell.

2. *Equation of state*

Having determined the rest-frame energy and baryon density, an equation of state (EoS) is needed as additional input to calculate the temperature T and baryochemical potential $\mu_{\rm B}$ for each cell. As the actual EoS for QCD matter is still not completely determined, this is an uncertainty within the calculation. For the present study we use a hadron-gas EoS with vacuum masses and without mean-field potentials (HG-EoS) [51, 52] following from hadronic chiral model calculations [53, 54]. The included hadrons agree with the degrees of freedom in UrQMD. However, this approach does not account for a phase transition to a deconfined phase as it is neither implemented in UrQMD nor in the hadron gas EoS. For heavy-ion collisions at SPS energies, where we find initial temperatures significantly above the expected critical temperature T_c, it will be also important to consider dilepton emission from cells with such high temperatures during the evolution of the medium. Therefore, we supplement the hadron-gas EoS with a partonic equation of state [55] which is obtained from a fit to lattice-QCD data of the form

$$\varepsilon/T^4 = \frac{c \cdot (1 + e^{-a/b})}{1 + e^{(T_c/T - a)/b}} \cdot e^{\lambda T_c/T}, \tag{15}$$

with fit parameters $a = 0.9979$, $b = 0.1163$, $c = 16.04157$ and $\lambda = 0.1773$ and critical temperature $T_c = 170\,$MeV. To ensure a smooth transition between the two EoS without any jumps in temperature (i.e., to avoid discontinuities in the evolution), the values of T from the lattice EoS are matched with the HG-EoS in the temperature range from 150-170 MeV and exclusively used above T_c.

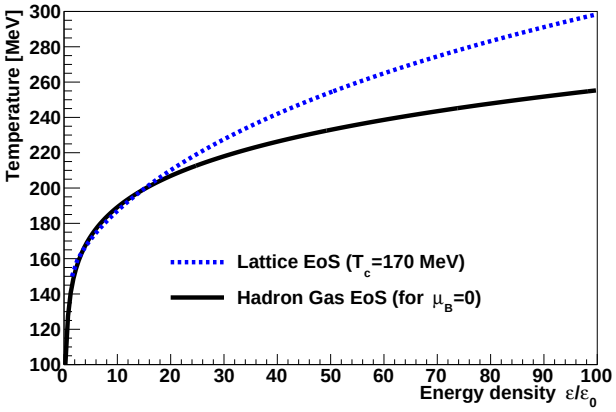

FIG. 1. (Color online) Comparison of the two equations of state used in our model, the hadron gas EoS [51] with UrQMD-like degrees of freedom (black line) and the Lattice EoS [55] to model the deconfined phase (blue line). We show the temperature dependence on the energy density (in units of normal nuclear-matter density, ε_0). While for the Lattice EoS $\mu_{\rm B} = 0$ intrinsically, we set the chemical potential to zero as well for the hadron gas EoS for reasons of comparison.

In Figure 1 a comparison of the relation between temperature and energy density is shown for the two equations of state used in the model. The hadron-gas EoS is represented by the black line and the lattice EoS by the blue dashed line. While for the lattice EoS $\mu_{\rm B} = 0$ is valid intrinsically, the baryon density and in consequence the chemical potential are set to zero in this plot for the hadron gas EoS for reasons of comparison. However, the rather moderate baryon chemical potential found at top SPS energy does not have a large impact on the relation between energy density and temperature and gives rise to a deviation from the curve for $\rho_{\rm B} = \mu_{\rm B} = 0$ of at maximum a few MeV. As observed from Fig. 1, both equations of state agree very well up to an energy density of roughly $15\varepsilon_0$, which corresponds to a temperature of

200 MeV. This implies that both EoS are dual in the region around the phase transition, guaranteeing a smooth cross-over transition when changing from the QGP EoS to the hadron-gas EoS across the phase transition.

The parametrization of the Rapp-Wambach spectral function [56], which will be used in this study for convenient and reliable application, is constructed such that the presence of baryonic matter enters via a dependence on an effective baryon density

$$\rho_{\mathrm{eff}} = \rho_{\mathrm{N}} + \rho_{\bar{\mathrm{N}}} + 0.5\,(\rho_{\mathrm{B}^*} + \rho_{\bar{\mathrm{B}}^*})\,. \tag{16}$$

It includes nucleons and excited baryons as well as their anti-particles. The reason not to take μ_{B} is that the interaction between the ρ and a baryon is the same as with an anti-baryon, i.e., it is not the net-baryon number that affects the electromagnetic current-current correlation function but the sum of baryons and anti-baryons. In our approach, we calculate the value of ρ_{eff} not via the EoS but directly from the cell's rest-frame.

3. Pion chemical potential

In full chemical equilibrium all meson chemical potentials are zero since the meson number is not a conserved quantity. When applying the EoS as described above, the explicit assumption is that in each cell we find a thermally and chemically equilibrated system. However, it has been shown that in transport models during the initial non-equilibrium stage – which is dominated by high energy densities – an over-dense pionic system is created and remains for significant time-scales due to the long relaxation time of pions [57, 58]. This is mainly caused by initial string fragmentation and resonances decaying into more than two final particles (e.g. $\omega \to 3\pi$) for which the back-reaction channel is not implemented. Also macroscopic approaches find non-zero μ_π after the number of pions is fixed at the chemical freeze-out but the system further cools down and expands [59]. The appearance of a finite μ_π has a large effect on the creation of ρ mesons and therefore on the thermal dilepton emission (see section II C). Therefore, though in general assuming chemical equilibrium, we exclude the pions from this assumption and extract a pion chemical potential in each cell via a Boltzmann approximation. The according relation for a relativistic gas is given by [60]

$$\mu_\pi = T \cdot \ln\left(\frac{2\pi^2 n_\pi}{g_\pi T m^2 \mathrm{K}_2\left(\frac{m}{T}\right)}\right), \tag{17}$$

with the pion density n_π in the cell, the pion degeneracy $g_\pi = 3$, and the Bessel function of the second kind, K_2. Other meson chemical potentials as, e.g., a kaon chemical potential are not considered in the present study, as the dependence of the ρ spectral function with regard to μ_K is negligible.

C. Dilepton emission rates

By assuming that the cells in our (3+1)-dimensional space-time grid are in local equilibrium (except for the finite μ_π) we can calculate the thermal emission from these cells. The dilepton emission is related to the imaginary part of the electromagnetic current-current correlation function [61, 62], $\mathrm{Im}\,\Pi_{\mathrm{em}}^{(\mathrm{ret})}$. The full expression for the dilepton emission rate per four-volume and four-momentum from a heat bath at temperature T and chemical potential μ_{B} takes the form [32]

$$\begin{aligned}\frac{\mathrm{d}N_{ll}}{\mathrm{d}^4x\mathrm{d}^4q} = &-\frac{\alpha_{\mathrm{em}}^2 L(M)}{\pi^3 M^2}\, f^{\mathrm{B}}(q\cdot U;T) \\ &\times \mathrm{Im}\,\Pi_{\mathrm{em}}^{(\mathrm{ret})}(M,\vec{q};\mu_B,T),\end{aligned} \tag{18}$$

where f^{B} denotes the Bose-distribution function and L the lepton phase-space factor,

$$L(M) = \sqrt{1-\frac{4m_\mu^2}{M^2}}\left(1+\frac{2m_\mu^2}{M^2}\right), \tag{19}$$

which reaches 1 rapidly above the threshold, given by twice the lepton mass.

To calculate invariant-mass spectra from equation (18) we integrate over four-volume and three-momentum

$$\frac{\mathrm{d}N_{ll}}{\mathrm{d}M} = \int \mathrm{d}^4x \frac{M\mathrm{d}^3\vec{p}}{p_0}\frac{\mathrm{d}N_{ll}}{\mathrm{d}^4x\mathrm{d}^4p} \tag{20}$$

In our case the integration over the four-volume simply reduces to a multiplication of the cell's four-volume.

1. Thermal ρ emission

There exist several approaches to calculate the in-medium spectral functions, e.g., by using empirical scattering amplitudes [63]. Here the ρ spectral function from hadronic many-body calculations by Rapp and Wambach [64] is used, which has proven a good agreement with experimental results at CERN-SPS and RHIC energies in previous studies [14, 15, 32]. In this approach, the hadronic part of the electromagnetic current-current correlator is saturated by light vector mesons according to the Vector Dominance Model (VDM). The correlator is hereby related to the ρ spectral function, respectively the propagator, as

$$\mathrm{Im}\,\Pi_{\mathrm{em}}^{(\mathrm{ret})} = \frac{(m_\rho^{(0)})^4}{g_\rho^2}\,\mathrm{Im}\,D_\rho^{(\mathrm{ret})}. \tag{21}$$

To determine the propagator, several contributions to the self-energy have to be considered, i.e., in this case the meson gas ($\Sigma_{\rho M}$) and nuclear matter effects ($\Sigma_{\rho B}$) as well as the in-medium $\rho\pi\pi$ width ($\Sigma_{\rho\pi\pi}$). This results in

$$D_\rho = \frac{1}{M^2 - (m_\rho^{(0)})^2 - \Sigma_{\rho\pi\pi} - \Sigma_{\rho M} - \Sigma_{\rho B}}. \tag{22}$$

For the present study we use a parametrization of the Rapp-Wambach spectral function [56] that has been checked against the full spectral function and proven to agree well, with a maximal deviation of up to 15% in the mass region around 0.4 GeV.

To arrive at the final yield $N_{\rho\to ll}$ we have to generalize (18) for a chemical off-equilibrium state with finite pion chemical potential. It is necessary to include an additional (squared) fugacity factor, which is in Boltzmann approximation

$$z_\pi^2 = \exp\left(\frac{2\mu_\pi}{T}\right). \tag{23}$$

The reason for this is that the above expression for the dilepton emission rate (18) is independent of the hadronic initial and final states as only chemical potentials of conserved charges are considered (for which $Q_i = Q_f$). However, since the pion number N_π is not a conserved quantity this assumption is no longer correct for $\mu_\pi \neq 0$ which means that generally $N_{\pi,i} - N_{\pi,f} \neq 0$.

2. *Multi pion emission*

While the ρ meson is expected to dominate the dilepton emission in the low invariant mass range up to $M = 1\,\mathrm{GeV}$, a continuum starts to develop above, and multi-pion interactions will contribute at higher masses.

As detailed in [65], the vector correlator at finite temperature takes the form

$$\Pi^V_{\mu\nu}(p,T) = (1-\varepsilon)\Pi^V_{\mu\nu}(p,0) + \varepsilon\Pi^A_{\mu\nu}(p,0) \tag{24}$$

with the mixing parameter $\varepsilon = T^2/(6F_\pi^2)$ (F_π: pion-decay constant). In this paper, we follow the same approach as presented in [14, 15], using

$$\begin{aligned}\Pi_V(p) =&(1-\varepsilon)z_\pi^4\Pi^{\mathrm{vac}}_{\mathrm{V},4\pi} + \frac{\varepsilon}{2}z_\pi^3\Pi^{\mathrm{vac}}_{\mathrm{A},3\pi}\\ &+\frac{\varepsilon}{2}(z_\pi^4+z_\pi^5)\Pi^{\mathrm{vac}}_{\mathrm{A},5\pi}\end{aligned} \tag{25}$$

according to vector/axial-vector correlators from tau-decay data provided by ALEPH [66]. The pion chemical potentials are implemented via the fugacity factor z_π. The two-pion piece, as well as the three-pion piece corresponding to the a_1 decay, $a_1 \to \pi + \rho$, have been excluded as they are already included via the ρ spectral function.

3. *Quark-gluon plasma emission*

The dilepton emission from the quark-gluon plasma has been considered to be one of the most promising probes for the formation of a deconfined phase. In such a QGP phase, a quark can annihilate with an anti-quark into a dilepton pair (via a virtual photon).

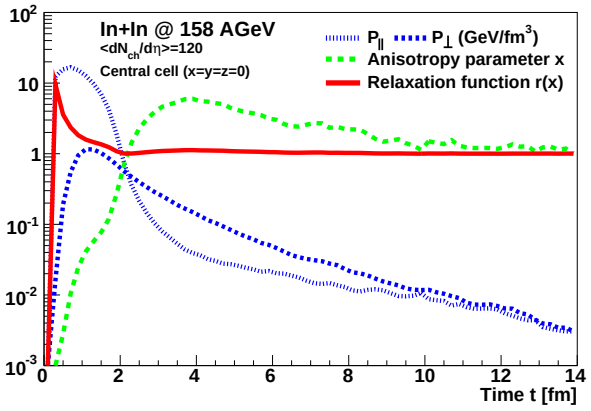

FIG. 2. (Color online) Longitudinal and transverse pressure for the central cell, as well as the anisotropy parameter $x = (P_\parallel/P_\perp)^{3/4}$ and the relaxation function $r(x)$ as defined in equation (14).

Here we use a corresponding spectral function extrapolated from lattice QCD correlators for three-momentum $\vec{q} = 0$ [67] and with a light-like limit, consistent with the leading order α_s photon production rate [32]. The emission rate per four-volume and four-momentum takes the form

$$\frac{\mathrm{d}N_{ll}}{\mathrm{d}^4x\mathrm{d}^4p} = \frac{\alpha_{\mathrm{em}}^2}{6\pi^3}\sum_q e_q^2\frac{\rho_{\mathrm{V}}(p_0,\vec{p},T)}{(p_0^2-\vec{p}^2)(\mathrm{e}^{p_0/T}-1)}, \tag{26}$$

where ρ_V denotes the vector spectral function. The current calculation assumes that the chemical potential is zero in the deconfined phase, i.e., that the quark and anti-quark distributions are equal.

For comparison also the pure perturbative quark-gluon plasma contribution is calculated. The rate has been evaluated for lowest order $q\bar{q}$ annihilation [68] as

$$\begin{aligned}\frac{\mathrm{d}N_{ll}}{\mathrm{d}^4x\mathrm{d}^4p} =&\frac{\alpha_{em}^2}{4\pi^4}\frac{T}{p}f^{\mathrm{B}}(p_0;T)\sum_q e_q^2\\ &\times\ln\frac{(x_-+y)\,(x_++\exp[-\mu_q/T])}{(x_++y)\,(x_-+\exp[-\mu_q/T])}\end{aligned} \tag{27}$$

with the expressions $x_\pm = \exp[-(p_0 \pm p)/2T]$ and $y = \exp[-(p_0+\mu_q)/T]$. Again, the quark chemical potential μ_q is zero for our considerations.

4. *Non-thermal ρ emission*

In addition to the thermal contribution, we also have to handle those cells where (i) the temperature is lower than 50 MeV (late stage), i.e., where it is not reasonable to assume a thermal emission and (ii) with no baryon but only meson content (in these cells the density is usually also quite low) which inhibits a determination of a local rest frame according to the Eckart description and

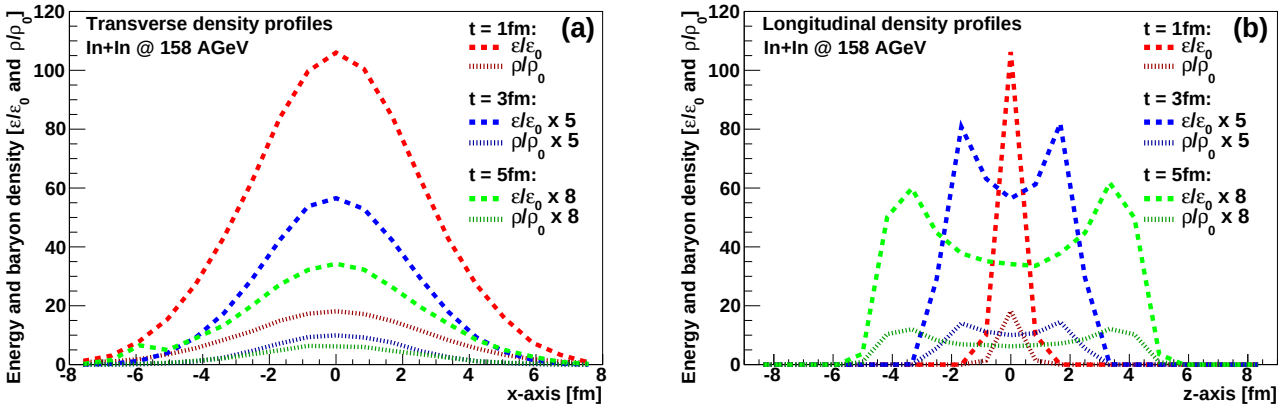

FIG. 3. (Color online) Transverse (a) and longitudinal (b) profiles of the energy density ε and the baryon density $\rho_{\rm B}$. The left plot shows the dependence of ε and $\rho_{\rm B}$ on the position along the x-axis, with y and z coordinates fixed to 0. The right plot shows the dependence along the z-axis (i.e., along the beam axis) with $x = y = 0$. The results are presented in units of the normal nuclear-matter densities, ε_0 and ρ_0.

in consequence one can not determine T and $\mu_{\rm B}$ in this way. In these cases we directly take the ρ^0 mesons from the UrQMD calculations. Within the transport approach they are mainly produced either via decay of heavy resonances (e.g. $N^*_{1520} \to \rho N$) or the reaction $\pi\pi \to \rho$. Production via strings is possible as well. For these ρ^0 mesons we apply a shining procedure that is conventionally used to calculate dilepton emission from a transport approach [69].

The mass-dependent width for the direct decay of a ρ^0 meson to a dilepton pair is expressed according to [70]

$$\Gamma_{V\to ll}(M) = \frac{\Gamma_{V\to ll}(m_\rho)}{m_\rho}\frac{m_\rho^4}{M^3}\cdot L(M), \qquad (28)$$

with the partial decay width at the ρ-pole mass $\Gamma_{\rho\to ll}(m_\rho)$; $L(M)$ denotes the lepton phase-space factor (19).

The according dilepton yield is then obtained by summing over all ρ^0 mesons from the low temperature cells,

$$\frac{dN_{ll}}{dM} = \frac{\Delta N_{ll}}{\Delta M} = \sum_{i=1}^{N_{\Delta M}}\sum_{j=1}^{N_\rho}\frac{\Delta t}{\gamma_\rho}\frac{\Gamma_{\rho\to ll}(M)}{\Delta M}. \qquad (29)$$

Here $\Gamma_{\rho\to ll}(M)$ is the electromagnetic decay width of the considered resonance defined in (28) and Δt is the length of a time step within our calculation. The factor γ_ρ^{-1} is introduced to account for the fact that the ρ meson lives longer in the center of mass system of the UrQMD calculation than in its rest frame in which the shining is applied (relativistic time dilation).

Note that we use the shining procedure only for cells for which we do *not* calculate the thermal emission, in consequence we avoid any form of double-counting.

III. RESULTS

The following calculations were performed with the coarse-graining approach as described above. To compare our results with the data recorded by the NA60 Collaboration, an input of 1000 UrQMD events with a random impact-parameter distribution restricted to $b < 8.5$ fm has been used, which corresponds to a value of $\langle {\rm d}N_{\rm ch}/{\rm d}\eta\rangle \approx 119$ in one unit of rapidity around mid-rapidity in the center-of-mass frame. This is very close to the value of $\langle {\rm d}N_{\rm ch}/{\rm d}\eta\rangle_{\rm exp} = 120$ which NA60 measured within their acceptance.

Note that several coarse-graining runs with different UrQMD events as input had to be performed to obtain enough statistics, especially for the non-thermal ρ contribution.

A. Space-time evolution

As dileptons are radiated over the whole space-time evolution of the nuclear reaction, it is important to model the dynamics as realistically as possible. When studying the electromagnetic radiation from the hot and dense phase of heavy-ion collisions, the thermodynamic properties of the fireball are the main input for the calculations.

We first investigate the anisotropic situation at the beginning of the collision. Figure 2 shows – for the central cell at the origin of our grid – the time evolution of the longitudinal and transverse pressure, $P_\parallel$ and $P_\perp$, together with the anisotropy parameter, x, and the relaxation function, $r(x)$, as defined in Eqs. (10) and (14). As one expects, the first time steps are characterized by high values of $P_\parallel$ while $P_\perp$ is rather negligible first but increases significantly later. Both quantities initially differ by three orders of magnitude. In the course of the evolution the values are approaching each other and become

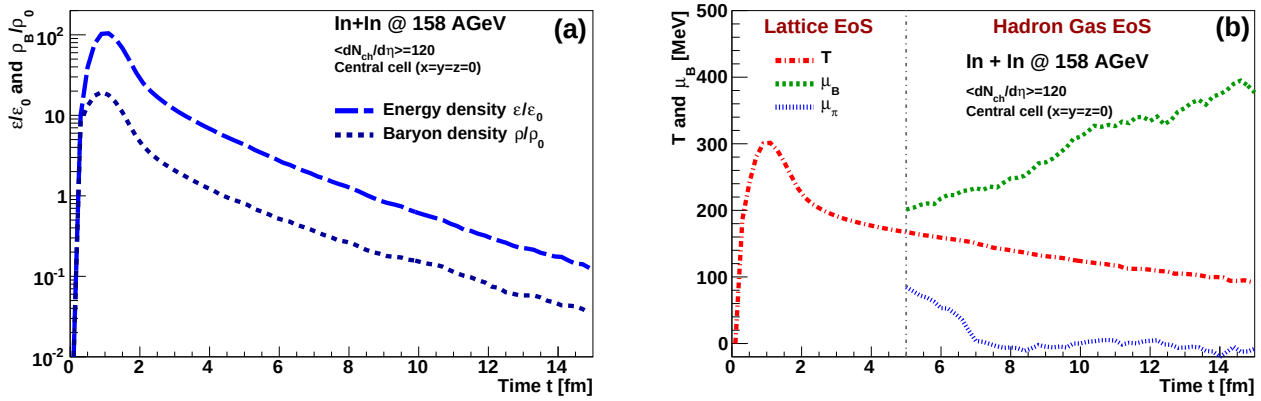

FIG. 4. (Color online) Left panel (a): Time evolution of the baryon density $\rho_{\rm B}$ (short dashed) and energy density ε (long dashed) for the cell at the center of the coarse-graining grid ($x = y = z = 0$). The results are given in units of the ground-state densities ε_0 and ρ_0. Right panel (b): Time evolution of the temperature T (red dash-dotted), baryon chemical potential $\mu_{\rm B}$ (green short dashed) and the pion chemical potential μ_π (blue dotted) in the central cell. The thin grey line indicates the transition from the Lattice EoS to the Hadron Gas EoS at the transition temperature of $T = 170\,$MeV.

equal around $t = 2\,\mathrm{fm}/c$. But they do not remain equal at later times but the perpendicular pressure then exceeds the longitudinal one by a factor 3-5 in the further development until they finally equalize around $t = 10\,\mathrm{fm}/c$. This finding agrees with previous studies of the kinetic equilibration within the UrQMD model [38]. When considering the influence of the pressure anisotropy on the local thermodynamic properties one has to bear in mind that according to (11) the realistic energy density in the cell is determined by the relaxation function $r(x)$. Its value drops rapidly from an initial value of 10 (i.e. the realistic isotropized energy density is here only 10% of the actual energy density in the cell) to 1 at $t = 2\,\mathrm{fm}/c$ and remains on that level. In consequence, the anisotropy does not significantly influence the thermodynamic properties in the cell after $2\,\mathrm{fm}/c$.

The transverse and the longitudinal profiles of the energy density ε and the baryon density ρ_B are presented in Figure 3. The left plot (a) shows the distribution of ρ and ε in dependence on the position along the x-axis whereas $y = z = 0$ and the right plot (b) shows the dependence on the z-position (i.e. along the beam axis) with $x = y = 0$. The results are plotted for three different time steps, at 1, 3 and $5\,\mathrm{fm}/c$ after the beginning of the collision. (Note that the results for $t = 3\,\mathrm{fm}/c$ and $5\,\mathrm{fm}/c$ are scaled up for better comparability.) The shape of the transverse profile looks almost identical at all times with a clear peak at $x = 0$, which is falling off smoothly on both sides at the more peripheral and less dense regions where consequently also less energy is deposited. However, both energy and baryon density decrease clearly in the course of time due to the expansion of the system. This expansion can directly be seen in the longitudinal profile on the right side. On the one hand, we see one clear peak structure at $t = 1\,\mathrm{fm}/c$ when the two nuclei still mostly overlap. However, at $t = 3\,\mathrm{fm}/c$ and $5\,\mathrm{fm}/c$ we observe a double-peak structure with maxima that sheer off from each other. A region of high ε and $\rho_{\rm B}$ is created in between when the two nuclei have traversed each other. Stopping effects have produced this hot and dense zone, whereas some remnants of the nuclei still fly apart with high velocity. As we can see from these profiles, the highest initial baryon and energy densities should be expected at the origin of our grid in the center of the collision. Indeed the time evolution of ε and ρ in Figure 4 (a) shows a rapid rise up to baryon and energy densities of 20 times respectively 100 times the ground state densities. The maxima are reached at a time of about $1.2\,\mathrm{fm}/c$ after the beginning of the collision and in the following the densities decrease again – first rapidly, then slower again. After application of the equation of state we observe a similar behavior for the time dependence of the temperature, with values of up to 300 MeV. It is important to bear in mind that we apply two different EoS here, a lattice EoS for temperatures above 170 MeV to mimic a Quark-Gluon-Plasma phase and a Hadron-Gas EoS for lower temperatures. As we see, a smooth transition in temperature between the two EoS is obtained around $t = 5\,\mathrm{fm}/c$, which one would have already expected from the fact that the EoS agree quite well for $T < 200\,$MeV. The baryo-chemical potential from the hadron gas EoS slowly rises from a value of 200 MeV at the transition time up to a maximum of 400 MeV in the course of the evolution. This increase is similar to the findings of [40] and caused by the stronger relative decline of the energy density compared to the baryon density. A different behavior can be observed for the pion chemical potential μ_π, which is around 100 MeV first and then drops to values around 0. This is unlike the findings of fireball approaches, where particle numbers are fixed at a freeze-out and the subsequent cooling of the system leads to a build-up of a finite pion chemical

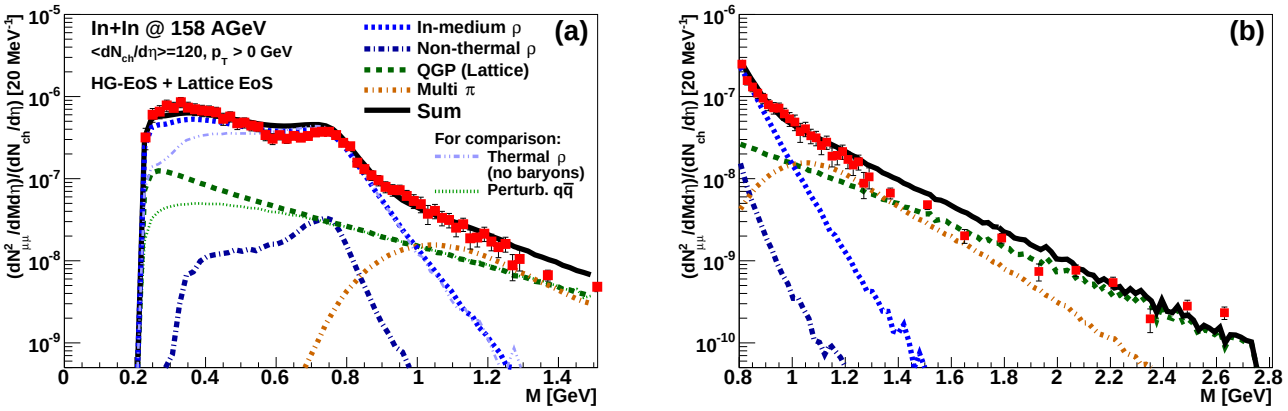

FIG. 5. (Color online) Invariant mass spectra of the dimuon excess yield in In+In collisions at a beam energy of 158 AGeV, for the low-mass region up 1.5 GeV (a) and the intermediate-mass regime up to 2.8 GeV (b). We show the contributions of the in-medium ρ emission according to the Rapp-Wambach spectral function [56] (blue short dashed), the contribution from the Quark-Gluon Plasma, i.e., $q\bar{q}$-annihilation, according to lattice rates [32, 67] (green dashed) and the emission from multi-pion reactions, taking vector-axial-vector mixing into account [15] (orange dash-dotted). Additionally a non-thermal transport contribution for the ρ is included in the yield (dark blue dash-dotted). Only left plot: For comparison the thermal ρ without any baryonic effects, i.e. for $\rho_{\rm eff} = 0$, is shown (violet dash-double-dotted) together with the yield from pure perturbative $q\bar{q}$-annihilation rates (green dotted). The results are compared to the experimental data from the NA60 Collaboration [11, 12, 71]

potential. The picture in our transport approach is completely different, as pions can be produced and absorbed over the whole evolution in the system.

As we see from the time evolution of the central cell, the temperature reaches values of 100 MeV even after a time of 15 fm/c. However, this is a special case and for most cells the temperature has already dropped beyond significance before. But in contrast to many approaches with a fixed lifetime of the fireball, here an underlying microscopic transport description is applied which takes into account that some singular cells still reach quite high temperatures and densities even after the usually assumed fireball lifetimes. The contribution to the dilepton yield from these few cells is, however, quite negligible.

B. Dilepton spectra

The next step is to investigate how the space-time evolution obtained by coarse-graining the transport simulations is reflected within the resulting dilepton spectra. It is hereby of particular interest whether and how the differences in the reaction dynamics as compared to the fireball parametrizations will be reflected in the $\mu^+\mu^-$-distributions as measurable in experiment (and whether one by this can discriminate between different scenarios of the fireball evolution).

In Figure 5 the resulting dimuon invariant-mass spectra from the coarse-graining calculations are compared to data from the NA60 Collaboration. There the dimuon excess yield in In+In collisions at a beam energy of $E_{\rm lab} = 158\,A$GeV with $\langle {\rm d}N_{\rm ch}/{\rm d}\eta\rangle = 120$ is shown, for the low-mass region up to $M = 1.5$ GeV (a) and the intermediate-mass regime up to 2.8 GeV (b). We show the contributions of the in-medium ρ emission, from the quark-gluon plasma, i.e., $q\bar{q}$-annihilation, and the emission from multi-pion reactions, taking vector-axial-vector mixing into account. The dilepton emission due to decays of ρ mesons from the low-temperature cells is included as well, but in the full p_t-integrated spectrum it is rather negligible compared to the other contributions. Comparison with the experimental data from the NA60 Collaboration [11, 71] shows a very good agreement of our theoretical result with their measurement. Only a slight tendency to underestimate the data in the invariant mass region from 0.2 to 0.4 GeV and a minor excess above the data in the pole region is observed. As the low-mass enhancement and the melting of the peak at the pole mass are mainly caused by the baryonic effects on the ρ meson spectral function and very sensitive to the presence of baryons and anti-baryons, this might be due to the fact that the baryon densities (respectively the baryon chemical potential) are still slightly too low in our approach. An additional modification of the spectral shape not considered here may also be caused by the ω-t-channel exchange. It has been found, however, to give only a small contribution to the total yield and is significant only for high transverse momenta [15]. Furthermore, one has to bear in mind as well that there is an uncertainty of up to 15% around $M \approx 0.4$ GeV between the parametrized spectral function and its full evaluation from thermal field theory which has been found in a full comparison between both approaches [56], as mentioned above. Taking this and the systematic uncertainties of the experimental data and of the model calculations into account, we conclude that the approach is fully able to

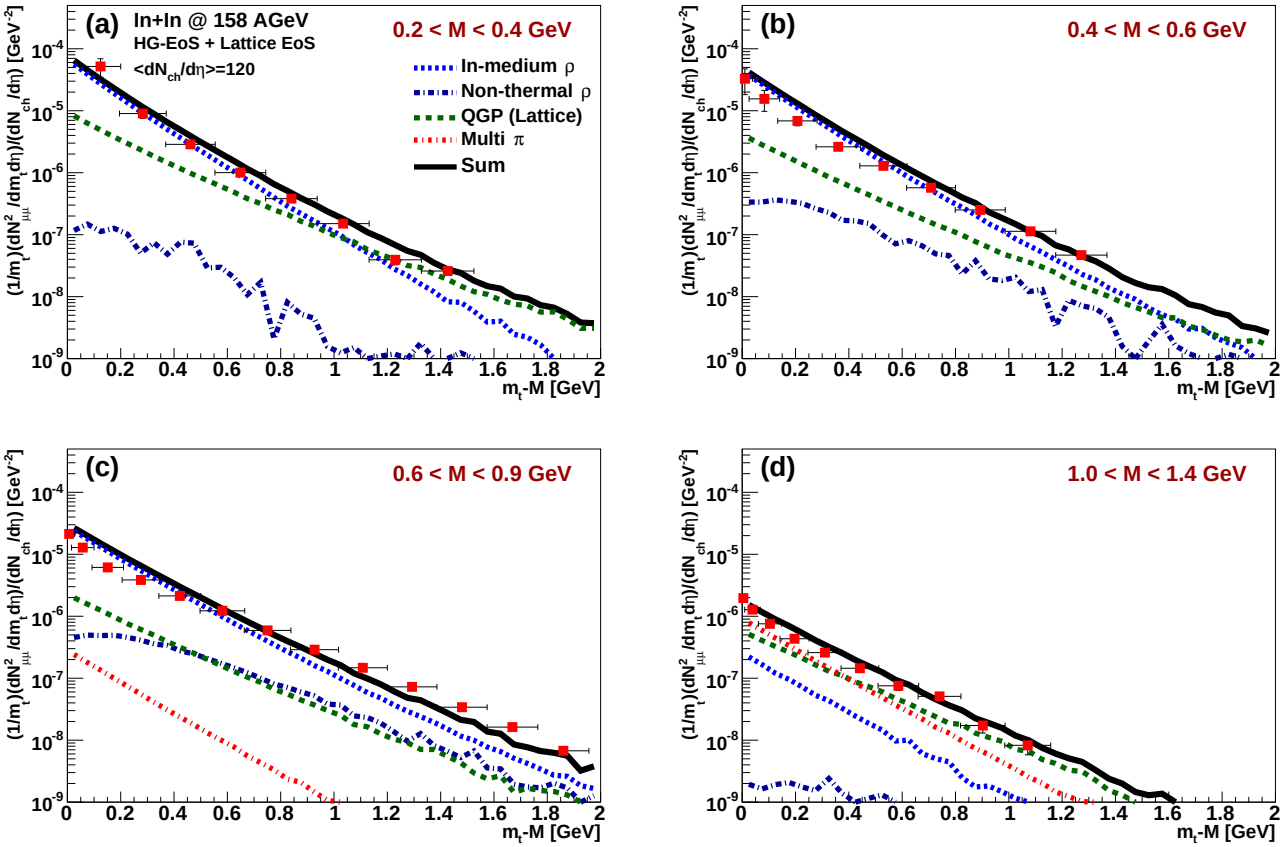

FIG. 6. (Color online) Transverse-mass ($m_t - M$) spectra in four different mass bins of the dimuon-excess yield in In+In collisions at a beam energy of 158 AGeV. We have the mass ranges 0.2 GeV $< M <$ 0.4 GeV (a), 0.4 GeV $< M <$ 0.6 GeV (b), 0.6 GeV $< M <$ 0.9 GeV (c) and the highest mass bin with 1.0 GeV $< M <$ 1.4 GeV (d). The different contributions are the same as in Figure 5. The results are compared to the experimental data from the NA60 Collaboration [72].

describe the total NA60 invariant mass spectrum with excellent accuracy.

To get an impression of the dominant role of baryon-induced medium modifications, the thermal ρ contribution assuming the absence of all baryons and anti-baryons (i.e., for $\rho_{\rm eff} = 0$) is also shown in Figure 5. In this case only meson-gas effects have an influence on the spectral function. Compared to the full in-medium ρ, it exhibits slightly more strength at the ρ meson's pole mass but is significantly below the experimental yield for $M < 0.6$ GeV by a factor of 2-5. Clearly, only the inclusion of interactions with baryonic matter can explain the low-mass dilepton excess, as has been noticed in previous studies [15].

Comparing the dilepton emission rates obtained from the lattice and from perturbative $q\bar{q}$-annihilation, both rates are identical for masses larger than 0.8 MeV, while the non-perturbative effects included in the lattice calculations give rise to a strong increase (up to a factor 3) of the yield at lower invariant masses. It is notable that the shape of the slope in the region $M > 1.5$ GeV is described with very good accuracy. This is important, as the hadronic contribution which dominates at lower masses becomes negligible here, and the yield is dominated by emission from the QGP phase. The intermediate-mass region is therefore a good benchmark for a correct description of the $q\bar{q}$ emission and allows for a reliable determination of the space-time averaged temperature without distortion from blue-shift effects due to flow (as is the case for effective slopes of p_t spectra) [73]. Note, however, that in contrast to the results from a fireball approach we here get a slightly larger contribution from the hadronic domain (ρ and multi-π), whereas in the fireball approach a more dominant QGP contribution is found, especially at low masses [15, 73]. This finding strengthens the hypothesis of duality between the hadronic and partonic dilepton emission in the transition temperature region between both phases [2].

In Figure 6 we present the transverse-mass ($m_t - M$) spectra in four different mass bins of the dimuon-excess yield in In+In collisions. The results are shown for mass bins of 0.2 GeV $< M <$ 0.4 GeV (a), 0.4 GeV $< M <$ 0.6 GeV (b), 0.6 GeV $< M <$ 0.9 GeV (c), and 1.0 GeV $< M <$ 1.4 GeV (d). The different contributions

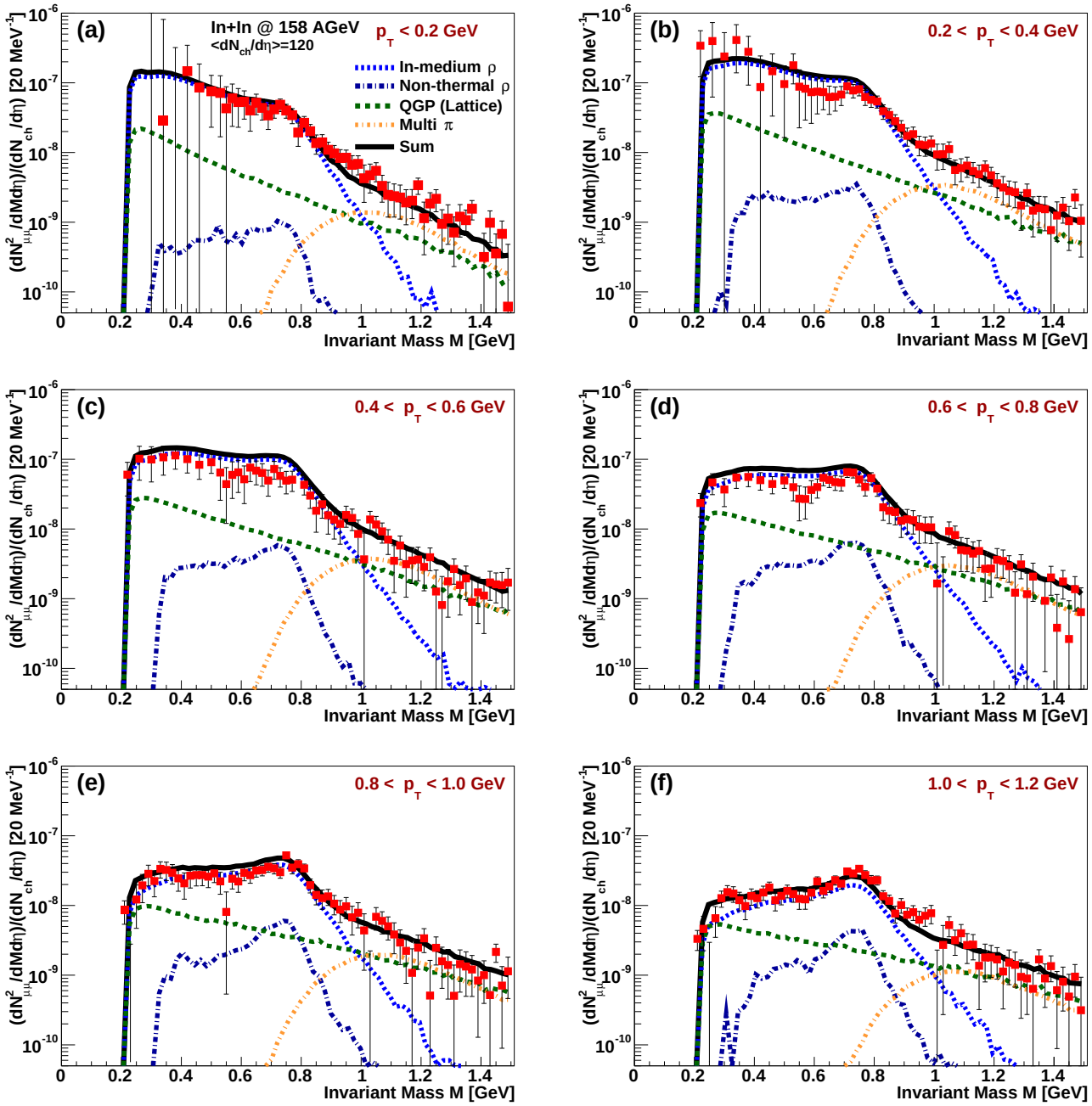

FIG. 7. The invariant mass spectra of the dimuon excess yield in In+In collisions at a beam energy of 158 AGeV, for the low-mass region as in the left plot of Figure 5, but for 6 different p_t-bins ranging from $p_t = 0$ to 1.2 GeV. The different contributions are the same as in Figures 5 and 6. The results are compared to the experimental data from the NA60 Collaboration [11].

are the same as in Figure 5. Comparison to the NA60 results [72] shows again a very good agreement. The calculations are in almost all cases within the error bars of the experimental data. Interesting is the dominance of the different contributions in certain transverse-mass respectively -momentum ranges. While the in-medium ρ dominates the spectra at low m_t for all but the highest mass bin, the QGP and the non-thermal ρ do not significantly contribute at low m_t but their relative strength increases when going to higher transverse mass.

Besides the invariant-mass and the transverse-mass spectra, we also studied the former as resolved in different p_t-slices. This analysis is of special interest as theoretical studies show that the medium modifications of the ρ spectral function depend strongly on the momentum. While a significant change of the spectral shape is predicted based on constraints from vacuum scattering and decay data at low momenta, this effect should

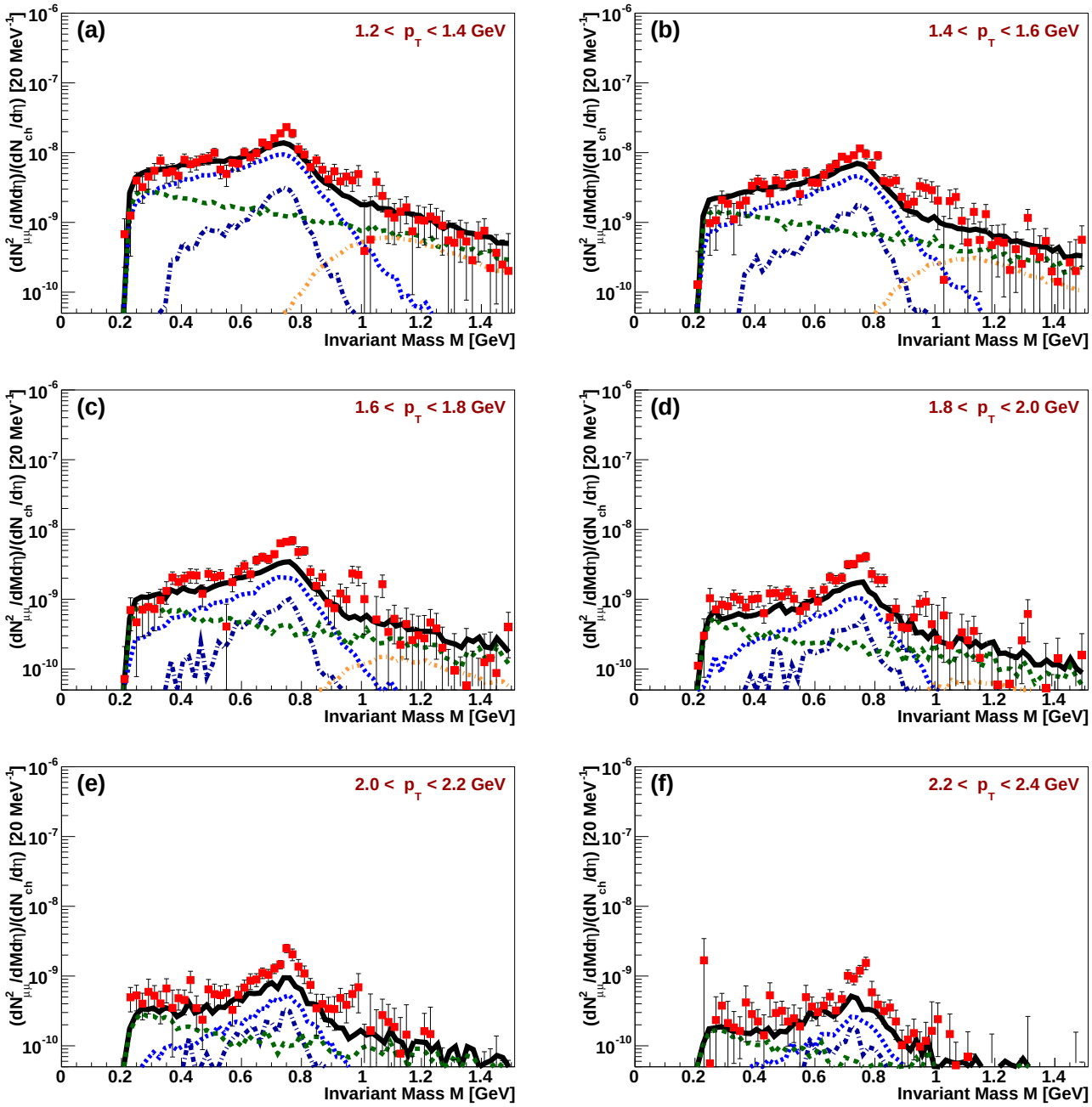

FIG. 8. Same as in Figure 7, but for higher p_t-bins ranging from $p_t = 1.2$ to 2.4 GeV. The different contributions are the same as in Figures 5 and 6. The results are compared to the experimental data from the NA60 Collaboration [11].

become less and less significant for higher momenta [6]. The resulting invariant mass spectra are shown in Figures 7 and 8, with 12 different plots representing the different p_t-bins with a width of $\Delta p_t = 200\,\text{MeV}$, ranging from the lowest values $0.0 \leq p_t \leq 0.2\,\text{GeV}$ up to the highest transverse momentum bin with $2.2\,\text{GeV} \leq p_t \leq 2.4\,\text{GeV}$. Our calculations once again agree with the data and especially show the clear momentum dependence of the ρ contribution in the region below the meson's pole mass. While for the lowest p_t-bin the yield in the mass range from 0.2 GeV to 0.4 GeV exceeds even the yield at the pole mass, this excess becomes increasingly smaller when we go to higher transverse momenta. For the highest p_t-bin the shape of the ρ in the invariant mass spectrum looks almost as in the vacuum. Besides, the relative contribution from the non-thermal transport ρ is increasing when going to higher transverse momentum. It is in addition noteworthy that also the non-thermal ρ, for which no explicit in-medium modifications are implemented in UrQMD, shows dynamically some p_t-dependence of the

spectral shape. However, this is not surprising since the transport model includes effects like resonance excitation, rescattering or reabsorption that can cause such a momentum dependent mass distribution, i.e., the spectral properties of the transport ρ include some medium effects and thus differ from those in the vacuum. The very same microscopic mechanisms, of course, also cause the medium modifications of the spectral functions within the thermal quantum-field theoretical models.

Yet, for p_t greater than 1.2 GeV the yield in the pole mass region of the ρ meson, i.e. at $M \approx 770\,\mathrm{MeV}$, is still not described fully. The experimental data show a more prominent and sharper peak structure than we find within our approach. Some of the "freeze-out" respectively "vacuum" ρ contribution might be missing in spite of including the non-thermal transport ρ.

In general it is interesting to see how the correct description of all the three different thermal contributions is necessary to achieve agreement with the data over the whole transverse momentum range. For example, at the lowest masses (below 0.4 GeV) the broadened ρ delivers the significant contribution for low p_t, while at higher p_t the emission from the deconfined phase dominates at these masses. This is another good benchmark that shows that we obviously describe the thermal emission quite realistically. Nevertheless, one also has to stress that the results for the total dilepton spectra obtained in the present study agree with the studies performed with fireball parametrizations, though the space-time evolution shows significant differences between the two models. This indicates that the time-integral nature of dilepton spectra to a large extent disguises the details of the reaction dynamics by averaging over volume and lifetime.

IV. CONCLUSIONS & OUTLOOK

In this paper we have presented a coarse-graining approach to the calculation of dilepton production in heavy-ion collisions. Using an ensemble of several events from transport calculations with the UrQMD model, we put the output on a space-time grid of small cells. By averaging the particle distribution in each cell over a large number of events and going into the local rest frame we can calculate the energy and baryon density and consequently temperature and chemical potential by introducing an equation of state. When the thermodynamic properties of the cell are known the corresponding thermal dilepton emission rates can be determined. With this procedure it is aimed to achieve a more realistic description of dilepton production in heavy-ion collisions. Since a complete non-equilibrium treatment of medium modifications is an extremely difficult task, the coarse-graining approach is intended as a compromise to apply in-medium spectral functions in combination with a microscopic description of the bulk evolution of a heavy-ion collision.

The agreement between our results for thermal dilepton invariant- and transverse-mass spectra and the experimental findings of the NA60 collaboration is very good. The coarse-graining study also confirms previous calculations with the same spectral function within a fireball approach [14, 15, 73]. However, it is remarkable that in spite of differences in the dynamics of the reaction, the final results are so similar in both approaches. The main distinctions are, in summary:

(i) The rise of large chemical potentials in the earlier stages of the reaction within the coarse-graining approach, while in the fireball model a finite μ_π shows up after the freeze-out.

(ii) A larger fraction of QGP dilepton contribution is found in the fireball model while we get less QGP and more hadronic emission when coarse-graining the microscopic dynamics.

(iii) The lifetime of the hot and dense system is about $7\,\mathrm{fm}/c$ in the fireball parametrization while we still find thermal emission even after much longer time of $15\,\mathrm{fm}/c$ in the present study. Note hereby that for the latter case T, μ_B (respectively ρ_{eff}) and μ_π are determined locally whereas the fireball model assumes global thermal equilibrium.

The obvious explanation for the agreement is that the dilepton spectra are only time-integrated results and therefore less significant with regard to the very details of the reaction evolution but rather the global scale of the dynamics, i.e., one is mainly sensitive to the average thermal properties of the system. The high-mass tail of the invariant mass spectrum, which is clearly dominated by the QGP emission (i.e. for $M > 1.5\,\mathrm{GeV}$) is a good example for this. It reflects the true average temperature of the source (without blue shifts as in the photon case) and was found to be roughly 205 MeV in fireball models. Looking at the details, one finds however that the QGP yield for very high masses over 2.5 MeV is larger in the coarse-graining, but the overall slope of the partonic emission is flatter so that the differences between the two approaches show up especially at lower masses. This can be explained by the fact that we have some very hot cells with temperatures above 300 MeV populating the yield at very high masses, while the initial temperature in the fireball is only 245 MeV. In contrast, the overall QGP emitting volume is larger in the fireball model due to the assumption of global equilibrium, while only a limited number of cells reaches above T_c in the coarse-graining approach. For lower masses, less QGP yield is counter-balanced by a larger hadronic contribution. This is not surprising, because the lower number of high-temperature cells corresponds to a larger fraction of low-temperature emission. A more detailed comparison beyond this will be addressed in a future work. However, it becomes already clear that there are several aspects which only show up in their combined effect in the dilepton spectra, so e.g. a smaller volume can be compensated by a longer lifetime of the fireball.

Nevertheless, in spite of the insensitivity with regard to the detailed reaction dynamics, we can also draw some conclusions by the agreement of the results from the fireball and coarse-graining model:

1. The large influence of baryons on the spectral shape of the ρ which is clearly responsible for the enhancement of the dilepton yield in the mass range $0.2\,\mathrm{GeV} < M_{\mu\mu} < 0.6\,\mathrm{GeV}$. The most significant modifications of the spectral function of the ρ are found at low momenta, in line with previous experimental and theoretical investigations.

2. Thermal emission from the QGP, at least in parts for temperatures significantly above the critical temperature T_c. Without this both models fail to fully explain the invariant mass spectrum at higher invariant masses.

3. Especially for the mass region above the ρ meson, i.e, for $1\,\mathrm{GeV} < M_{\mu\mu} < 2\,\mathrm{GeV}$ the results also strengthen the hypothesis of quark-hadron duality, i.e., that the thermal emission rates are dual in the temperature range around the transition temperture between the partonic and the hadronic phase.

For the future the latter two points deserve further investigation, especially with regard to the transition from the hadronic to the partonic phase. The present results show that it will be hard to definitely determine details of the evolution of the reaction by means of dilepton spectra. But the question whether electromagnetic probes can give hints for the creation of a QGP phase or whether duality prohibits to discriminate between hadronic and partonic emission in the transition region might be clarified in theoretical studies at lower collision energies as, e.g., covered by the Beam-Energy Scan program at the Relativistic Heavy Ion Collider (RHIC) and the future FAIR facility (with $E_\mathrm{lab} = 8 - 35\,\mathrm{AGeV}$). But also a full understanding of the medium modifications of hadron properties and the possible restoration of chiral symmetry has not yet been obtained and further theoretical and experimental studies are desirable, especially exploring the high-μ_B region of the QCD phase diagram.

Considering the aspects mentioned above, the fundamental applicability of the coarse-graining approach for all kinds of collision energies opens the possibility for a broad variety of future investigations. For low-energy heavy-ion collisions as investigated at the GSI SIS (HADES) it offers a unique option, since an application of conventional hydrodynamic or fireball models seems not reasonable here and microscopic transport models failed to give an unambiguous explanation of the observed dilepton spectra at low bombarding energies. The expected high baryon densities in these cases make a detailed study of the thermodynamic properties interesting.

ACKNOWLEDGMENTS

The authors especially thank Ralf Rapp for providing his spectral function and for many fruitful discussions. This work was supported by the Hessian Initiative for Excellence (LOEWE) through the Helmholtz International Center for FAIR (HIC for FAIR), the Federal Ministry of Education and Research (BMBF) and the Helmholtz Research School for Quark-Matter Studies (H-QM).

[1] T. Hatsuda and S. H. Lee, Phys. Rev. C **46**, 34 (1992).
[2] R. Rapp and J. Wambach, Adv. Nucl. Phys. **25**, 1 (2000).
[3] G. Brown and M. Rho, Phys. Rept. **363**, 85 (2002).
[4] R. S. Hayano and T. Hatsuda, Rev. Mod. Phys. **82**, 2949 (2010).
[5] R. Rapp, J. Wambach, and H. van Hees, in R. Stock (ed.), *Relativistic Heavy Ion Physics*, vol. 23 of *Landolt-Börnstein - Group I Elementary Particles, Nuclei and Atoms*, 134–175 (Springer, Berlin, 2010).
[6] S. Leupold, V. Metag, and U. Mosel, Int. J. Mod. Phys. E **19**, 147 (2010).
[7] L. H. Xia, C. M. Ko, L. Xiong, and J. Q. Wu, Nucl. Phys. A **485**, 721 (1988).
[8] C. Gale and K. L. Haglin, in R. C. Hwa and X.-N. Wang (eds.), *Quark-Gluon Plasma 3* (World Scientific, Singapore, 2004), arXiv: hep-ph/0306098.
[9] R. Arnaldi et al. (NA60 Collaboration), Phys. Rev. Lett. **96**, 162302 (2006).
[10] R. Arnaldi et al. (NA60 Collaboration), Phys. Rev. Lett. **100**, 022302 (2008).
[11] R. Arnaldi et al. (NA60 Collaboration), Eur. Phys. J. C **61**, 711 (2009).
[12] R. Arnaldi et al. (NA60 Collaboration), Eur. Phys. J. C **59**, 607 (2009).
[13] G. Agakichiev et al. (CERES Collaboration), Phys. Rev. Lett. **75**, 1272 (1995).
[14] H. van Hees and R. Rapp, Phys. Rev. Lett. **97**, 102301 (2006).
[15] H. van Hees and R. Rapp, Nucl. Phys. A **806**, 339 (2008).
[16] K. Dusling, D. Teaney, and I. Zahed, Phys. Rev. C **75**, 024908 (2007).
[17] J. Ruppert, C. Gale, T. Renk, P. Lichard, and J. I. Kapusta, Phys. Rev. Lett. **100**, 162301 (2008).
[18] S. A. Bass, M. Belkacem, M. Bleicher, M. Brandstetter, L. Bravina, et al., Prog. Part. Nucl. Phys. **41**, 255 (1998).
[19] M. Bleicher, E. Zabrodin, C. Spieles, S. A. Bass, C. Ernst, et al., J. Phys. G **25**, 1859 (1999).
[20] W. Ehehalt and W. Cassing, Nucl. Phys. A **602**, 449 (1996).
[21] O. Buss, T. Gaitanos, K. Gallmeister, H. van Hees, M. Kaskulov, et al., Phys. Rept. **512**, 1 (2012).
[22] W. Cassing, E. Bratkovskaya, R. Rapp, and J. Wambach, Phys. Rev. C **57**, 916 (1998).
[23] B. Schenke and C. Greiner, Phys. Rev. C **73**, 034909 (2006).
[24] B. Schenke and C. Greiner, Phys. Rev. Lett. **98**, 022301 (2007).
[25] B. Schenke and C. Greiner, Nucl. Phys. A **785**, 170

(2007).
[26] E. Bratkovskaya, W. Cassing, and O. Linnyk, Phys. Lett. B **670**, 428 (2009).
[27] W. Cassing and E. Bratkovskaya, Nucl. Phys. A **831**, 215 (2009).
[28] H. Barz, B. Kampfer, G. Wolf, and M. Zetenyi, Open Nucl. Part. Phys. J. **3**, 1 (2010).
[29] O. Linnyk, E. Bratkovskaya, V. Ozvenchuk, W. Cassing, and C. Ko, Phys. Rev. C **84**, 054917 (2011).
[30] J. Weil, H. van Hees, and U. Mosel, Eur. Phys. J. A **48**, 111 (2012).
[31] J. Weil, U. Mosel, and V. Metag, Phys. Lett. B **723**, 120 (2013), 1210.3074.
[32] R. Rapp, Adv. High Energy Phys. **2013**, 148253 (2013).
[33] D. Teaney, J. Lauret, and E. Shuryak (2001), arXiv: nucl-th/0110037.
[34] T. Hirano and K. Tsuda, Phys. Rev. C **66**, 054905 (2002).
[35] P. F. Kolb and U. Heinz, in R. C. Hwa and X.-N. Wang (eds.), *Quark-Gluon Plasma 3* (World Scientific, Singapore, 2004).
[36] C. Nonaka and S. A. Bass, Phys. Rev. C **75**, 014902 (2007).
[37] G. Vujanovic, C. Young, B. Schenke, R. Rapp, S. Jeon, et al., Phys. Rev. C **89**, 034904 (2014).
[38] L. Bravina, E. Zabrodin, M. I. Gorenstein, S. Bass, M. Belkacem, et al., Phys. Rev. C **60**, 024904 (1999).
[39] E. Santini, J. Steinheimer, M. Bleicher, and S. Schramm, Phys. Rev. C **84**, 014901 (2011).
[40] P. Huovinen, M. Belkacem, P. J. Ellis, and J. I. Kapusta, Phys. Rev. C **66**, 014903 (2002).
[41] H. Petersen, M. Bleicher, S. A. Bass, and H. Stöcker (2008), 0805.0567.
[42] `http://www.urqmd.org`.
[43] C. Eckart, Phys. Rev. **58**, 919 (1940).
[44] P. Braun-Munzinger, J. Stachel, J. Wessels, and N. Xu, Phys. Lett. B **365**, 1 (1996).
[45] J. Cleymans, D. Elliott, H. Satz, and R. Thews, Z. Phys. C **74**, 319 (1997).
[46] A. Andronic, P. Braun-Munzinger, and J. Stachel, Nucl.Phys. A **772**, 167 (2006).
[47] L. Bravina, M. I. Gorenstein, M. Belkacem, S. Bass, M. Bleicher, et al., Phys. Lett. B **434**, 379 (1998).
[48] L. Bravina, M. Brandstetter, M. I. Gorenstein, E. Zabrodin, M. Belkacem, et al., J. Phys. G **25**, 351 (1999).
[49] W. Florkowski and R. Ryblewski, Phys. Rev. C **83**, 034907 (2011).
[50] W. Florkowski, M. Martinez, R. Ryblewski, and M. Strickland, Nucl. Phys. A **904-905**, 803c (2013).
[51] D. Zschiesche, S. Schramm, J. Schaffner-Bielich, H. Stöcker, and W. Greiner, Phys. Lett. B **547**, 7 (2002).
[52] H. Petersen, J. Steinheimer, G. Burau, M. Bleicher, and H. Stocker, Phys. Rev. C **78**, 044901 (2008).
[53] P. Papazoglou, D. Zschiesche, S. Schramm, J. Schaffner-Bielich, H. Stöcker, et al., Phys. Rev. C **59**, 411 (1999).
[54] D. Zschiesche, G. Zeeb, and S. Schramm, J. Phys. G **34**, 1665 (2007).
[55] M. He, R. J. Fries, and R. Rapp, Phys. Rev. C **85**, 044911 (2012).
[56] R. Rapp (2014), private communication.
[57] M. Kataja and P. Ruuskanen, Phys. Lett. B **243**, 181 (1990).
[58] H. Bebie, P. Gerber, J. Goity, and H. Leutwyler, Nucl. Phys. B **378**, 95 (1992).
[59] P. F. Kolb and R. Rapp, Phys. Rev. C **67**, 044903 (2003).
[60] J. Sollfrank, P. Koch, and U. W. Heinz, Z. Phys. C **52**, 593 (1991).
[61] E. L. Feinberg, Nuovo Cim. A **34**, 391 (1976).
[62] L. D. McLerran and T. Toimela, Phys. Rev. D **31**, 545 (1985).
[63] V. L. Eletsky, M. Belkacem, P. Ellis, and J. I. Kapusta, Phys. Rev. C **64**, 035202 (2001).
[64] R. Rapp and J. Wambach, Eur. Phys. J. A **6**, 415 (1999).
[65] M. Dey, V. Eletsky, and B. L. Ioffe, Phys. Lett. B **252**, 620 (1990).
[66] R. Barate et al. (ALEPH Collaboration), Eur. Phys. J. C **4**, 409 (1998).
[67] H.-T. Ding, A. Francis, O. Kaczmarek, F. Karsch, E. Laermann, et al., Phys. Rev. D **83**, 034504 (2011).
[68] J. Cleymans, J. Fingberg, and K. Redlich, Phys. Rev. D **35**, 2153 (1987).
[69] K. Schmidt, E. Santini, S. Vogel, C. Sturm, M. Bleicher, et al., Phys. Rev. C **79**, 064908 (2009).
[70] G.-Q. Li, C. M. Ko, G. E. Brown, and H. Sorge, Nucl. Phys. A **611**, 539 (1996).
[71] H. J. Specht (NA60 Collaboration), AIP Conf.Proc. **1322**, 1 (2010).
[72] S. Damjanovic et al. (NA60 Collaboration), Nucl. Phys. A **783**, 327 (2007).
[73] R. Rapp and H. van Hees (2014), arXiv: 1411.4612 [hep-ph].